

Article

Temperature and Ambient Band Structure Changes in SnO₂ for the Optimization of Hydrogen Response

Petros-Panagis Filippatos ^{1,2,*}, Anastasia Soultati ¹, Nikolaos Kelaidis ¹, Dimitris Davazoglou ¹, Maria Vasilopoulou ¹ , Charalampos Drivas ³, Stella Kennou ³ and Alexander Chroneos ^{4,5,*} 

¹ Institute of Nanoscience and Nanotechnology (INN), National Center for Scientific Research Demokritos, Agia Paraskevi, 15310 Athens, Greece

² Faculty of Engineering, Environment and Computing, Coventry University, Priory Street, Coventry CV1 5FB, UK

³ Department of Chemical Engineering, University of Patras, 26504 Patras, Greece

⁴ Department of Electrical and Computer Engineering, University of Thessaly, 38221 Volos, Greece

⁵ Department of Materials, Imperial College, London SW7 2AZ, UK

* Correspondence: petpanfilippatos@gmail.com (P.-P.F.); alexander.chroneos@imperial.ac.uk (A.C.)

Abstract: Tin dioxide (SnO₂) is one of the most used materials for sensing applications operating at high temperatures. Commonly, “undoped SnO₂” is made by precursors containing elements that can have a deleterious impact on the operation of SnO₂ sensors. Here, we employ experimental and theoretical methods to investigate the structural properties and electronic structure of the rutile bulk and surface SnO₂, focusing on unintentional doping due to precursors. Unintentional doping from precursors as well as intrinsic doping can play an important role not only on the performance of gas sensors, but also on the properties of SnO₂ as a whole. The theoretical calculations were performed using density functional theory (DFT) with hybrid functionals. With DFT we examine the changes in the electronic properties of SnO₂ due to intrinsic and unintentional defects and we then discuss how these changes affect the response of a SnO₂-based gas sensor. From an experimental point of view, we synthesized low-cost SnO₂ thin films via sol–gel and spin-coating processes. To further enhance the performance of SnO₂, we coated the surface with a small amount of platinum (Pt). The crystalline structure of the films was analyzed using x-ray diffraction (XRD) and scanning electron microscopy (SEM), while for the determination of the elements contained in the sample, X-ray photoelectron spectroscopy (XPS) measurements were performed. Furthermore, we investigated the effect of temperature on the band structure of SnO₂ in air, in a vacuum and in nitrogen and hydrogen chemical environments. To optimize the response, we used current–voltage characterization in varying environments. The aim is to associate the response of SnO₂ to various environments with the changes in the band structure of the material in order to gain a better understanding of the response mechanism of metal oxides in different pressure and temperature environments. We found that the resistance of the semiconductor decreases with temperature, while it increases with increasing pressure. Furthermore, the activation energy is highly affected by the environment to which the thin film is exposed, which means that the thin film could respond with lower energy when exposed to an environment different from the air.

Keywords: tin dioxide; sensors; DFT; experiments



Citation: Filippatos, P.-P.; Soultati, A.; Kelaidis, N.; Davazoglou, D.; Vasilopoulou, M.; Drivas, C.; Kennou, S.; Chroneos, A. Temperature and Ambient Band Structure Changes in SnO₂ for the Optimization of Hydrogen Response. *Inorganics* **2023**, *11*, 96. <https://doi.org/10.3390/inorganics11030096>

Academic Editor: Zemin Zhang

Received: 2 November 2022

Revised: 13 February 2023

Accepted: 22 February 2023

Published: 27 February 2023



Copyright: © 2023 by the authors. Licensee MDPI, Basel, Switzerland. This article is an open access article distributed under the terms and conditions of the Creative Commons Attribution (CC BY) license (<https://creativecommons.org/licenses/by/4.0/>).

1. Introduction

Metal oxides are the most common materials used for sensing applications due to their crystallite size and physicochemical properties. Due to the evolution of the hydrogen economy, it is currently of great importance to fabricate devices that operate in extreme environments and are able to detect a possible leakage of this fuel. Hydrogen is characterized by flammability and the difficulty involved in storing and detection, as it is colorless,

tasteless and odorless. Tin dioxide is one of the few semiconductors that are used for hydrogen detection with high efficiency.

SnO_2 is one of the most commonly used materials in gas sensors due to its high response to many different gases, its easy fabrication and low cost [1]. Moreover, SnO_2 is used in many optoelectronic applications such as photovoltaics and light emitting diodes, as it combines both high electrical conductivity and optical transparency [2]. The common oxides based on tin are stannic oxide (SnO_2) and stannous oxide (SnO); however, other oxides, such as Sn_3O_4 , which are less stable, can also be fabricated [3]. Rutile is the most common SnO_2 polymorph (tetragonal with a space-group symmetry of $P4_2/mnm$). In rutile, the Sn atoms are six-fold coordinated to three-fold coordinated oxygen atoms [4]. SnO_2 is considered to be a wide bandgap (3.6 eV), n-type semiconductor. Although the applications of tin oxide vary in many fields, its stoichiometry causes low intrinsic carrier concentration and low charge mobility due to donor defects such as oxygen vacancies [5]. Apart from applications in gas sensors, SnO_2 is widely used in lithium-ion batteries and catalysts and is used as a precursor for the indium–tin oxide films (ITO) used as transparent electrons [6,7]. Many studies have investigated the effects of the grain size of SnO_2 on sensor sensitivity [8,9]. On an industrial scale, tin oxide films are deposited either by sputtering, by atmospheric pressure chemical vapor deposition (APCVD), by oxidizing SnCl_4 vapors with water and/or alcohol vapors or by applying the sol–gel spin coating technique. For the APCVD, chemicals are brought to the heated substrate as vapors and the oxide film is formed. The film's chemical evaporation temperature is highly connected to the reaction kinetics and to the loss of chemicals. Although this factor has been addressed in the literature (for example [10]), the effect of the concentration and the nature of the precursor has not been systematically considered. The most commonly used oxidizers for SnO_2 fabrication are methanol and water [9,11]. Both oxidizers lead to the formation of SnO_2 films with high transparency, but alcohol is known to enhance their conductivity [12]. This improved conductivity was related to the larger grain size exhibited by films grown by alcohol-containing gas phases [12].

While most of the studies pay attention only to the type of the gas that the sensor can detect, it is of great importance to investigate how the physical environment affects the nature of the sensing material. More specifically, many sensors should be able to operate in extreme environments such as vacuum conditions or a range of temperatures that are not stable. In this paper, we paid attention to the correlations between the intrinsic structural defects inherent in the precursors and remaining in the SnO_2 after annealing. Electronic structure calculations were performed to investigate the structural, optical and electronic influences that are caused by the substitution of Sn and O with C ions and by the effect of interstitial C atoms, which is a common defect in SnO_2 . Furthermore, incorporation of the Cl atom in interstitial and substitutional sites is discussed. Chlorine is included in the majority of the precursors of SnO_2 , i.e., SnCl_4 and $\text{SnCl}_2 \cdot 2\text{H}_2\text{O}$. Most of the studies focus only on the undoped, perfect material, while in our study we investigated the potential effect of the impurities that are introduced due to the process followed. The DFT calculations provide significant data on how changes in the electronic structure can be an advantage or disadvantage in terms of the response of the semiconductor towards different environments. Additionally, XRD and SEM measurements were also performed to compare structural and morphological alterations under different growth conditions. XPS (X-ray photoelectron spectroscopy) and UPS (ultraviolet photoelectron spectroscopy) measurements were used to investigate the states near the valence band maximum (VBM), the work function in every case and the kinds of unintentional dopants contained in the films. With this process, the band-structure changes are determined. For conductance measurements, the samples were positioned in a measurement chamber. With a computer-controlled measurement system, it is possible to control both the temperature of the samples and the gas atmosphere in the measurement chamber during the operations. In this way, we predicted the changes in the electronic properties resulting from changes in the band-structure, due to the temperature and pressure environment used.

2. Results

2.1. Theoretical

Here, we considered SnO₂ in the rutile tetragonal structure (P4₂/mmm, space group number 136). The calculated lattice parameters are $a = b = 4.717 \text{ \AA}$ and $c = 3.189 \text{ \AA}$, which were in good agreement with the experimentally determined values [13,14]. Here, we used one atom of carbon and chlorine in 48 atoms of SnO₂ (about 2% doping). This doping level was consistent with the experimental study of Hong et al. [15], who examined different carbon concentrations (1%, 5% and 10%) and found that carbon at a concentration of 1% produces high-quality films with saturated magnetization. They also indicated that the carbon atoms are inserted both in the surface and the bulk material. For our calculations, the amount of 2% was chosen in order to have results comparable to the amount of the carbon that is predicted from x-ray photoelectron spectroscopy and comparable to the amount chlorine that is contained from the precursor. Lower doping concentrations for our hybrid DFT simulations would be more time consuming. They also indicated that the carbon atoms are inserted both in the surface and in the bulk material [16]. We considered the carbon atom in either an interstitial or substitutional position on the Sn site (refer to Figure 1a,b). In the case of C_{Sn}: SnO₂ (Figure 1a), we calculated that the distance from the nearest oxygen atom is 1.27 Å, while for the interstitial case (Figure 1b), it is 1.28 Å. Additionally, in Figure 1c we predicted that carbon could enter oxygen sites and that the site was 2.13 Å from the nearest Sn atoms. For the Cl doping cases, regarding the substitutional doping, it was calculated that the nearest Sn atom was located at 2.37 Å (Figure 1d); for the interstitial position (Figure 1e), the nearest O is at 1.86 Å, and the nearest Sn is at a distance of 2.57 Å. Lastly, the interstitial position of the Sn atom in the structure was found to be 2.02 Å from the nearest O.

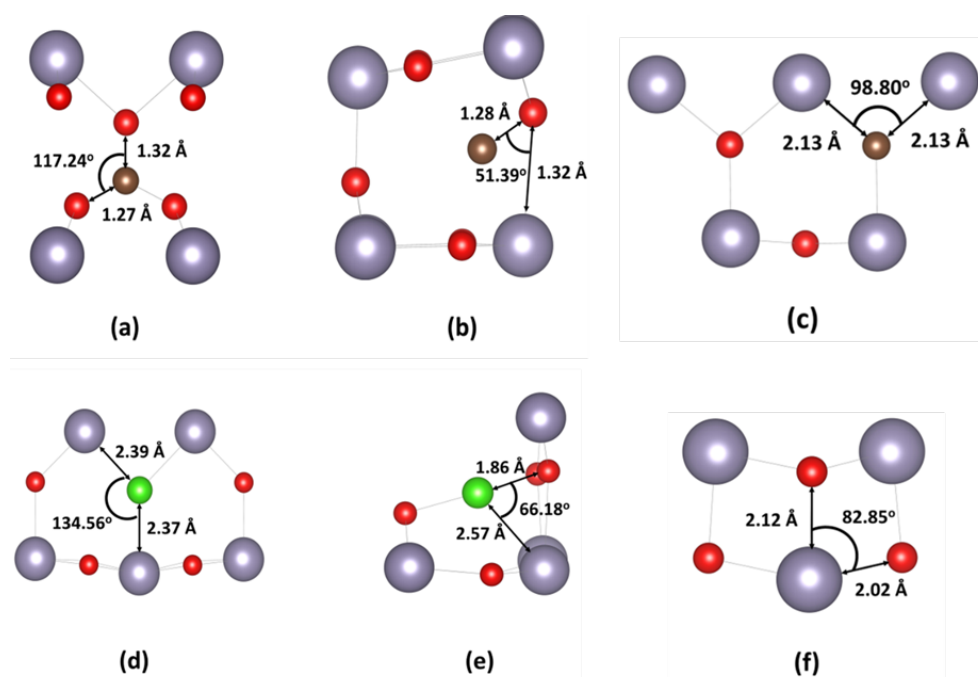


Figure 1. The doped cases examined: (a) C in Sn site, (b) C interstitial, (c) C as O substitutional (d) Cl interstitial, (e) Cl as O substitutional and (f) Sn interstitial.

For every defect case, the density of states (DOS) and the partial DOS (PDOS) are computed and presented in Figure 2. Notably, the PBE0 hybrid functional used here predicts the bandgap (3.35 eV) for the undoped SnO₂ (Figure 2e) in excellent agreement with the experimental value determined here (3.4 eV) and in previous studies (3.7 eV) [16]. Figure 2a shows the C_{Sn}: SnO₂ structure. The introduction of C creates additional energy states near the valence band, which in turn results in a bandgap reduction to 2.9 eV.

Generally, as predicted in previous work, the C substitutional creates additional states near the valence band in wide bandgap oxides [17]. Similarly, the carbon interstitial (Figure 2b) creates additional free states near the conduction band without a significant change to the bandgap value. As we show, carbon is a substance that is included on the surface of the semiconductor and so its simulation on the electronic structure is of great importance. It is also predicted that states form near the VBM (refer also to the UPS measurements in the experimental section). Cl (Figure 2c,e) is also a common dopant in most tin precursors and affects the electrical properties of the films [18,19]. The chlorine in the precursors of tin oxide supports the valence-controlled semiconductor model, where chlorine cations occupy oxygen sites, leading to free electrons that originate from the 5-s orbital of the Sn atom [20]. Using DFT in Figure 2d,e, we investigated the effect of chlorine as an oxygen substitutional and interstitial in the lattice. The substitutional chlorine (Figure 2d) favors the creation of additional states in the valence band and reduces the bandgap to a value of 2.8 eV. On the other hand, the interstitial incorporation of chlorine (Figure 2e) results in a band gap of 2.9 eV, and this time, states arise in the VBM. These states are created due to the hybridization of O-2p with Cl-3p. Lastly, we examined the electrical properties of the intrinsic defects of SnO₂, the Sn interstitial and the O vacancy (Figure 2f,g). Tin interstitials tend to reduce the bandgap and create gap states. From the above, it is assumed that both carbon and chlorine do not significantly affect the band gap at these concentrations but give rise to states that can be seen near the valence and the conduction band edges, which affects the conductivity of the thin film.

To better understand the influence of the precursor dopants on the SnO₂ films, the refractive index of the defective and pure structure was simulated. In Figure 3, the real part of the complex refractive index function represents light diffusion through the material. The imaginary part yields the extinction coefficient, which translates to beam losses due to the interaction with the material. For the undoped tin dioxide, the refractive index in zero frequency was computed at 1.40, which is lower than the experimental value due to the DFT underestimation of the electrical and optical properties [21]. The carbon substitutional in tin position does not change the refractive index compared to the undoped material (Figure 3a). In the interstitial case (Figure 3b), there is a slight increase in the refractive index (1.50) compared to the undoped material. It is seen that for a photon energy between 2 and 3.7 eV, the real part of the refractive index of the carbon substitutional is higher than that of the interstitial. Looking at the same range for the imaginary part, this phenomenon is reversed, and the imaginary part for the interstitial is higher than the substitutional. Oxygen substitution with a carbon atom was also examined and the refractive index was compared with the interstitial. The present results predict that in the energy range from 1.5 eV to 5 eV, the real part of the index is higher in C_o while the imaginary part is lower. Conversely, in Figure 4, the refractive index of the chlorine-doped structure does not change significantly compared to the undoped SnO₂. Lastly, in Figure 5a,b, the refractive index of the tin interstitial and oxygen vacancy was computed. The increase in the refractive index in the lower energies was attributed to the hybridized states between tin and oxygen.

In Figure 6a,b we present the bulk and surface SnO₂, while in Figure 6c,d we show the hydrogen interstitial and the minimum energy molecular adsorption system. The key quantity to evaluate the adhesive property of gas sensors is the adsorption energy, which is defined as the reversible energy required to discrete the system into an undoped surface and an adsorbed hydrogen molecule. When this energy is negative, then the configuration of the adsorbed site is stable, and the process is exothermic, while when it is positive, the process is endothermic. The molecule will not be adsorbed from this plane. We predicted the O_{2C} (bridge) site to be the most energetically favorable, with an $E_{\text{ads}} = -0.42$ eV.

The bandgap length and the large density of states at the conduction and valence band edges are the key parameters that affect the thermal and electrical properties of SnO₂. We predicted the DOS and pDOS for the bulk and surface structures as presented in Figure 7a,b, respectively. To tackle the bandgap underestimation problem, we employed the hybrid PBE0 functional, which provided a value of 3.35 eV, in good agreement with the reported

experimental value of 3.7 [22]. As we predicted, the Fermi level was computed inside the bandgap, categorizing the pristine SnO_2 as a semiconducting material. From the DOS plot, we can see that O-2p mainly forms the valence band which ranges from 0 to -7 eV, while the conduction band arises by the contribution of Sn-s and Sn-p orbitals as we have also described in previous studies [14,23]. To better understand the interaction of the hydrogen atom and molecule with the (110) surface of the SnO_2 , the electronic structure in Figure 7c,d was analyzed. We predicted that the O_{2c} site would be the most energetically advantageous position for H_2 adsorption; hence, we used this position in our analysis. There are notable changes in the DOS of the SnO_2 after H_2 adsorption. While adsorbed on the surface, the DOS shows a left shift towards lower energy values. From this analysis it can also be found that the DOS of SnO_2 with the adsorbed H_2 is broadened, which indicates that, due to orbital hybridization, chemical bonds are formed. These bandgap changes might be the mechanism that changes the conductance of SnO_2 when exposed to hydrogen gas.

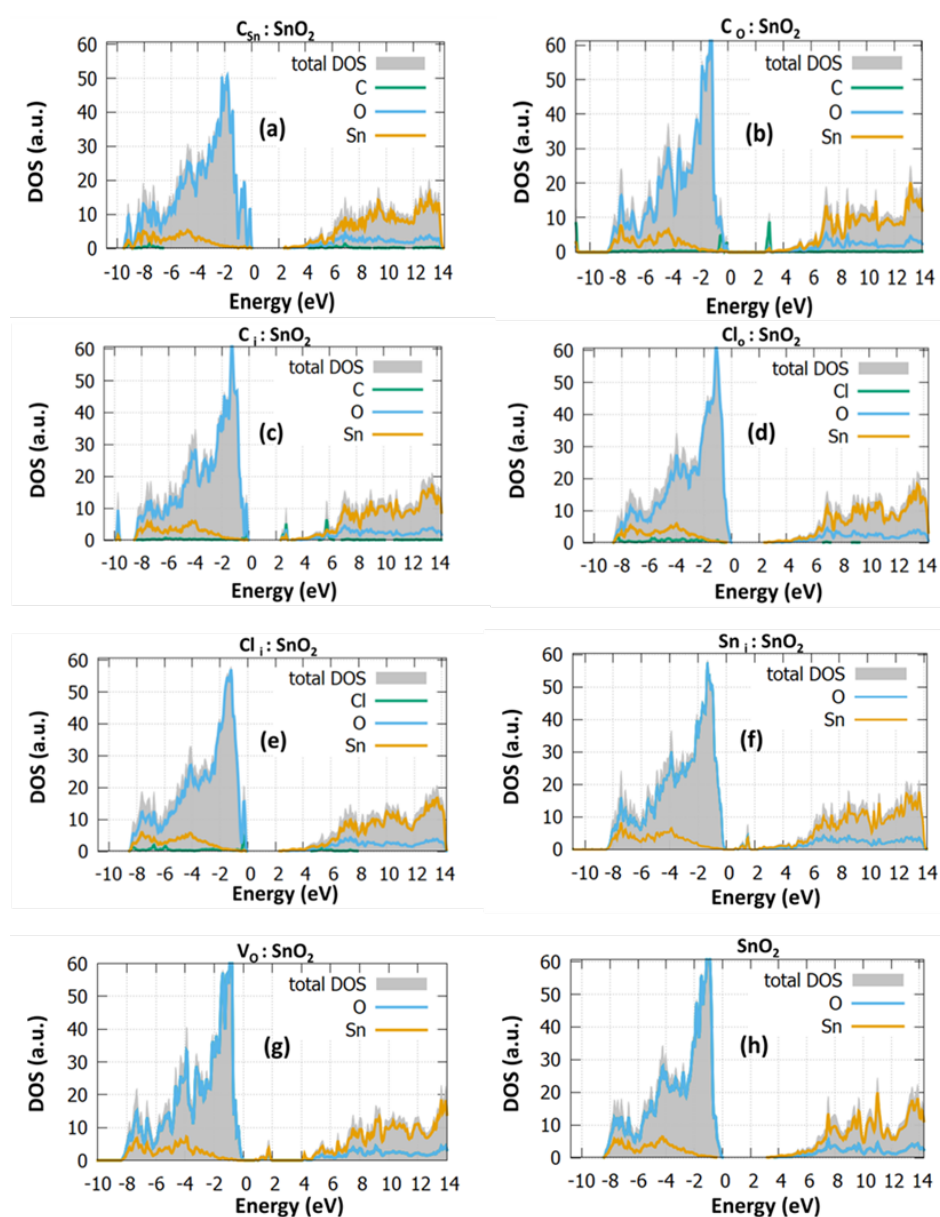


Figure 2. The total density of states (DOS) and the projected density of states (PDOS) of (a) $\text{C}_{\text{Sn}}: \text{SnO}_2$, (b) $\text{C}_{\text{O}}: \text{SnO}_2$, (c) $\text{C}_{\text{i}}: \text{SnO}_2$ (d) $\text{Cl}_{\text{O}}: \text{SnO}_2$ [14], (e) $\text{Cl}_{\text{i}}: \text{SnO}_2$ [14], (f) $\text{Sn}_{\text{i}}: \text{SnO}_2$, (g) $\text{V}_{\text{O}}: \text{SnO}_2$ and (h) undoped SnO_2 .

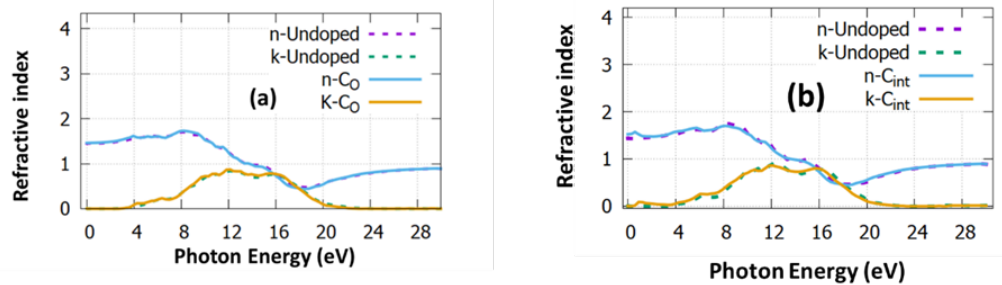


Figure 3. The refractive index of (a) C_O : SnO_2 and (b) C_i : SnO_2 .

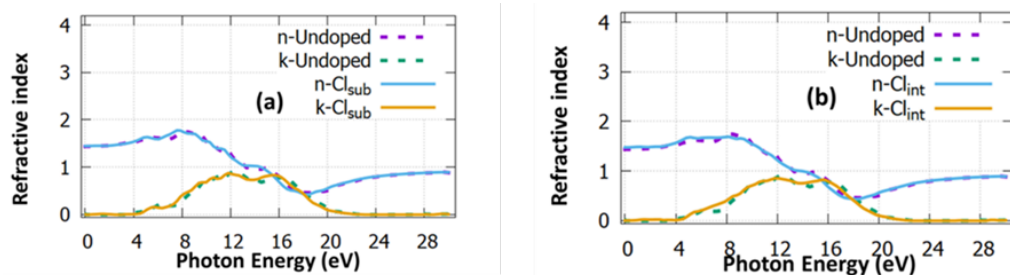


Figure 4. The refractive index of (a) Cl_{Sn} : SnO_2 and (b) Cl_I : SnO_2 .

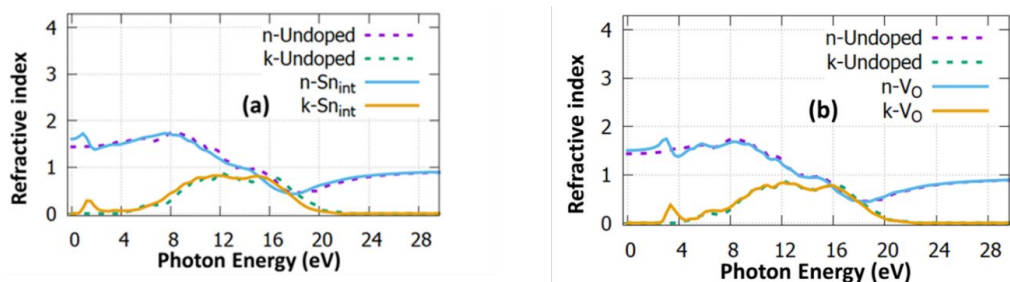


Figure 5. The refractive index of (a) Sn_I : SnO_2 and (b) V_O : SnO_2 .

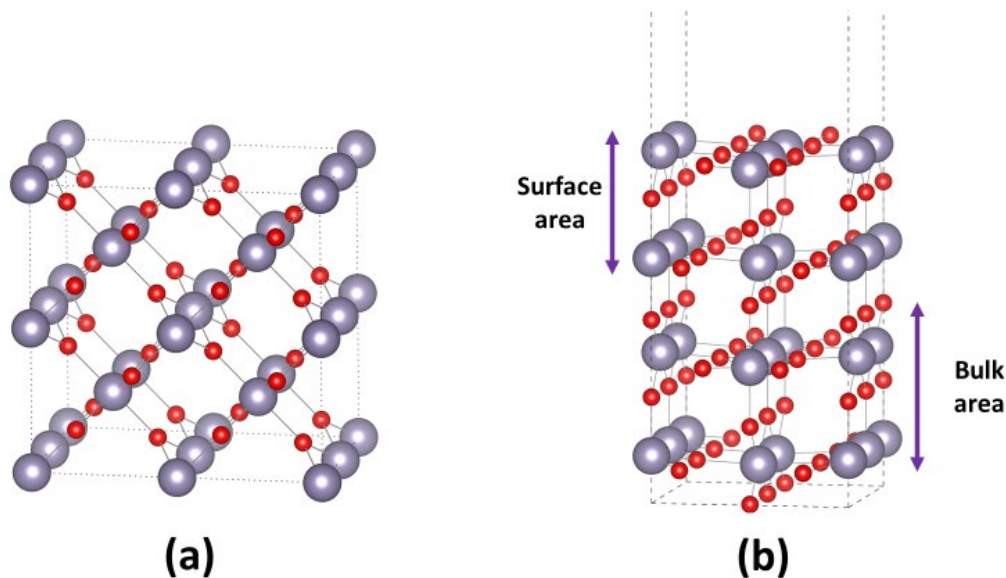


Figure 6. Cont.

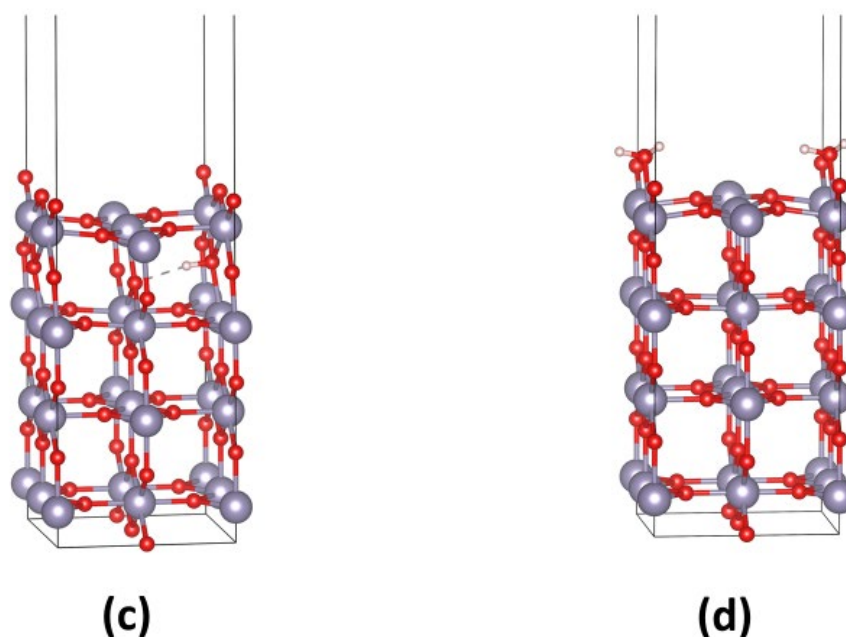


Figure 6. (a) The supercell, (b) the (110) surface model used, (c) the hydrogen interstitial in the (110) surface and (d) the bridge site adsorption on the (110) surface.

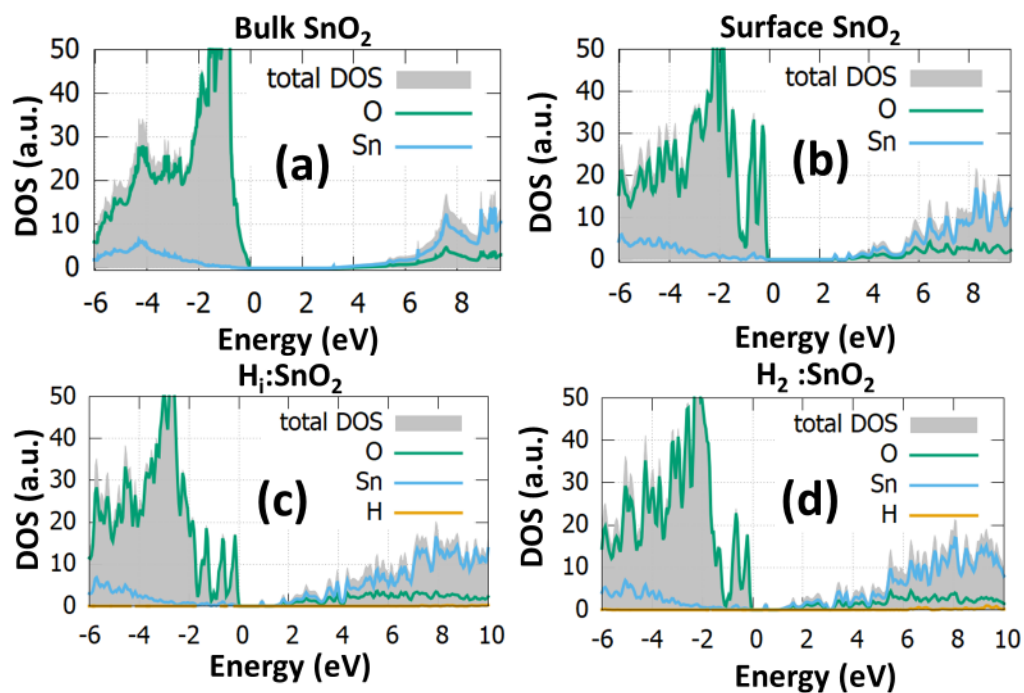


Figure 7. The DOS for the (a) bulk SnO_2 , (b) the (110) surface, (c) the hydrogen interstitial in the (110) surface and (d) the bridge site adsorption on the (110) surface.

2.2. Structural Characterization

Continuing with the morphological study of the structures (Figure 8), the surface of the two different SnO_2 cases were investigated using scanning electron microscopy images. In Figure 8a, the spin coating of the SnO_2 was performed at 1000 rpm, while in Figure 8c, the spin coating was under 3000 rpm. It is seen that the two structures exhibit a similar morphology. It is seen that generally the spin coating technique produces very thin SnO_2 films. More specifically, at 1000 rpm, the height of the sample was predicted to be

45 nm (Figure 8b). In Figure 8d, the rectangular area of the sample with one spin-coating is presented, when the angular speed is 3000 rpm.

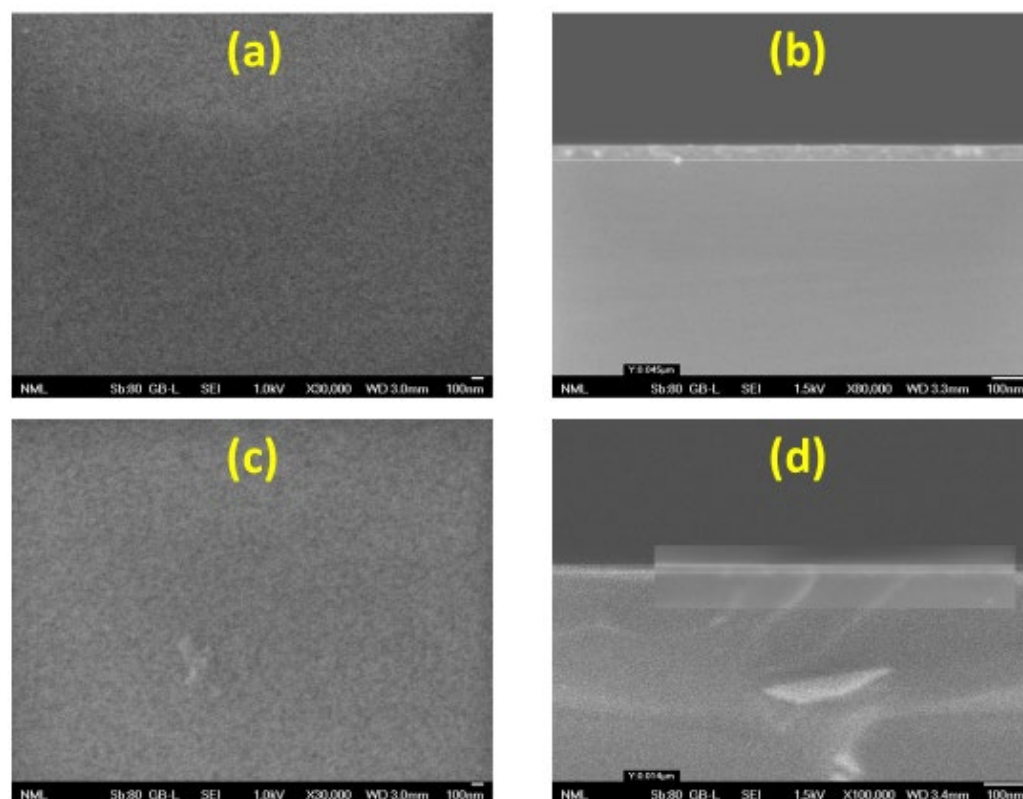


Figure 8. The SEM images for SnO₂ fabricated with ethanol via the sol-gel/spin-coating method: (a) the surface morphology for a 1000 rpm spin coating, (b) a cross-sectional image for a 1000 rpm spin coating, (c) the surface morphology for a 3000 rpm spin coating and (d) a cross-sectional image for a 3000 rpm spin coating.

Figure 9 illustrates the AFM and SEM cross-sectional images of the undoped SnO₂ that underwent ten-fold spin coating. Focusing on the AFM figure reveals important information about the morphology and the roughness. Specifically, it is seen that a nanoripple morphology is created by ten-fold spin coating, while the undoped SnO₂ had a roughness of 5.98 nm. From the SEM cross-sectional image, the size of the thin film that underwent ten-fold spin coating was calculated at 70 nm. The SnO₂ surface shows a fine and uniform distribution of nanoaggregates. Here, it was observed that, in the case of the undoped SnO₂, more spin-coatings result in a less rough sample. The morphology as well as the film thickness are highly connected to the response of the semiconductor towards different environments. Specifically, a difference in roughness translated to a change in the surface of the material and thus the active area, which is highly connected to the response properties of the material.

To investigate the SnO₂-based sensor structure, we used XRD (Figure 10). The XRD showed that the diffraction peaks arise at 26.7°, 33.8°, 37° and 52.2°, which corresponds to the (110), (101) and (200) facets. These peaks are in good agreement with the reported peaks of the tetragonal rutile structure of SnO₂ [24].

2.3. Electronic Characterization

From the wide scan survey spectra, Figure 11, the photoelectron peaks of Sn, C, O and Cl were detected for all the samples. Detailed scans of the most prominent photoelectron peak of each element present were taken to have an insight into their chemical state, and quantitative analysis was performed after the area of the peaks was measured upon

utilizing a Shirley background, summarized in Table 1. The O/Sn ratio is about 1.7 for all the samples, so the stoichiometry of the tin oxide is $\text{SnO}_{1.7}$. All samples have a 0.75 nm layer of carbon contamination on top of them. Figure 11a shows the Sn 3d region. The Sn 3d consists of two main peaks due to spin orbit splitting (S.O.S.). The Sn 3d_{5/2} and Sn 3d_{3/2} are located at a BE of 486.8 and 495.2 ± 0.1 eV, respectively, indicating the presence of SnO_2 . In Figure 11b, the C 1s region is shown. In all the spectra, a wide asymmetric peak can be seen, which is deconvoluted to four distinct carbon species constraining their full width at half maximum (FWHM) to be equal amongst them. The carbon species detected are C-C (285 eV), C-O (286.5 eV), C=O (288.5 eV) and carbonates (290 eV). As with the C 1s region, a single asymmetric peak can be seen for the O 1s region, Figure 11d, and deconvolution was performed. Three peaks were used, corresponding to O-Sn, -OH/ CO_x and organic oxygen. Figure 11c depicts the Cl 2p. A wide peak around 199 eV is present in all the spectra attributed to chloride species, most likely from the Sn precursor. In Table 1 the results from a quantitative analysis from the XPS are summarized. From the XPS we predicted that there is carbon contamination on the surface of the film with 0.75 nm thickness.

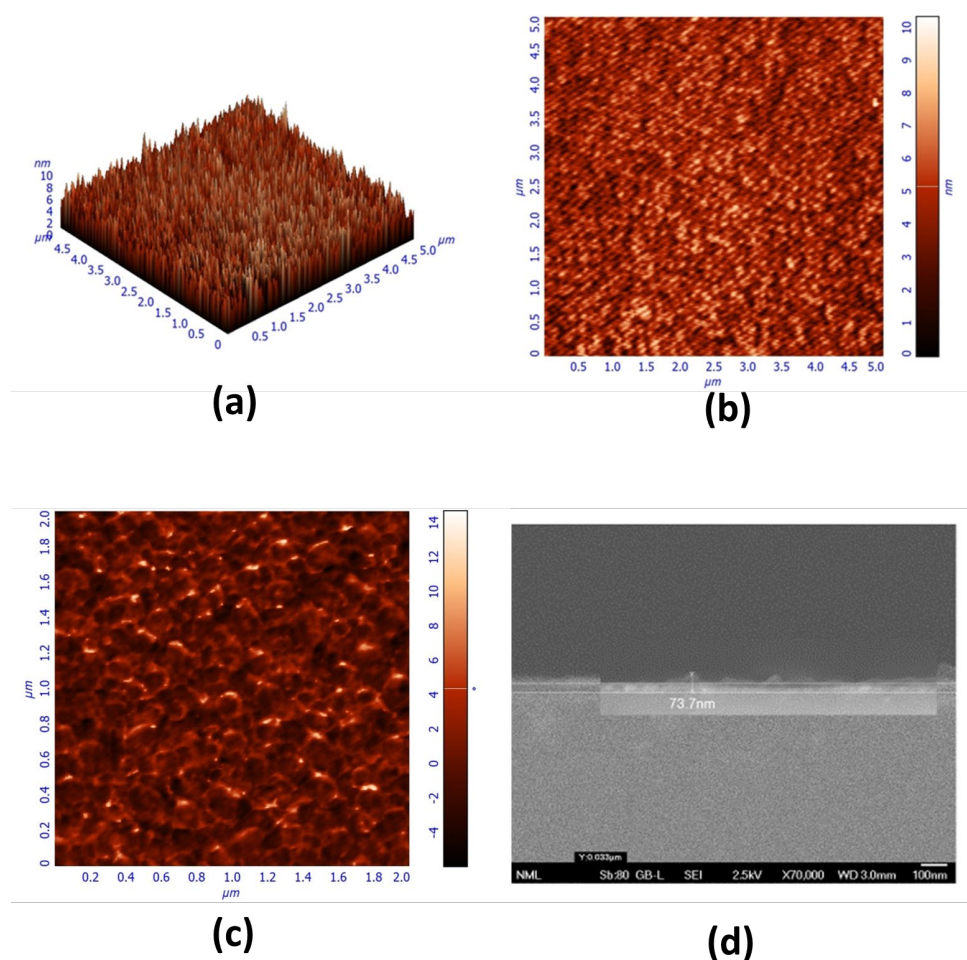


Figure 9. (a) The AFM of the side view, (b,c) the AFM from the top view from different scales and (d) the cross section of the undoped sample.

2.4. Electrical Characterization

The SnO_2 films here show typical semiconductor behavior according to their electrical conductivity σ , which increases with the sample heating temperature T_h , with more carriers being generated as discussed above (Figure 12). By measuring current voltage under different conditions, we optimized the response of the semiconductor. Especially for the gas sensors, the literature does not extend to exposure to various physical and chemical environments, so in order to investigate other potential applications as well as to understand

the band structure changes in different environments, it is of great importance to perform electrical characterization under different temperature and pressure conditions. In this paper, the I–V characteristics were determined for SnO₂ in three different environments: dry air (Figure 12a), a 0.01 Torr vacuum (Figure 12b) and 1000 ppm of hydrogen gas (Figure 12c). The current-voltage (I–V) characteristics for voltages between –10 and +10 V showed a strong non-linearity for the sample with Al electrodes up to 200 °C. In different chemical environments, it is clear that the form of the I–V significantly changes, which was expected due to the response of the sample to oxygen and hydrogen gases.

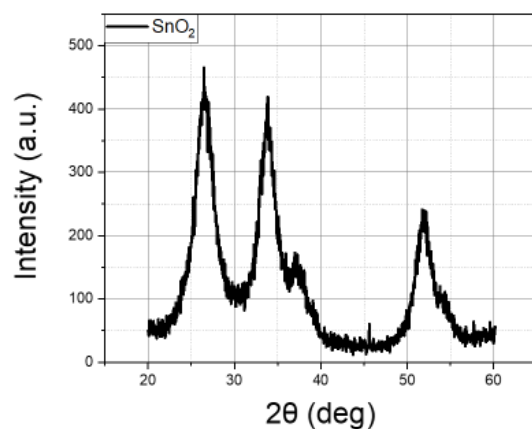


Figure 10. The XRD pattern for SnO₂.

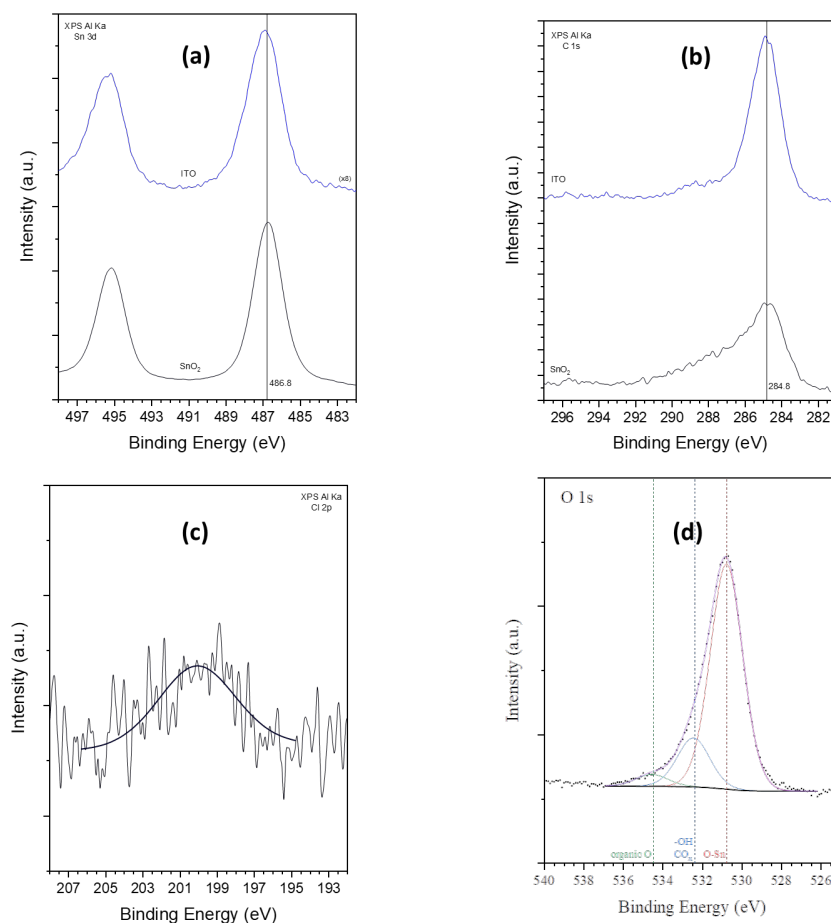
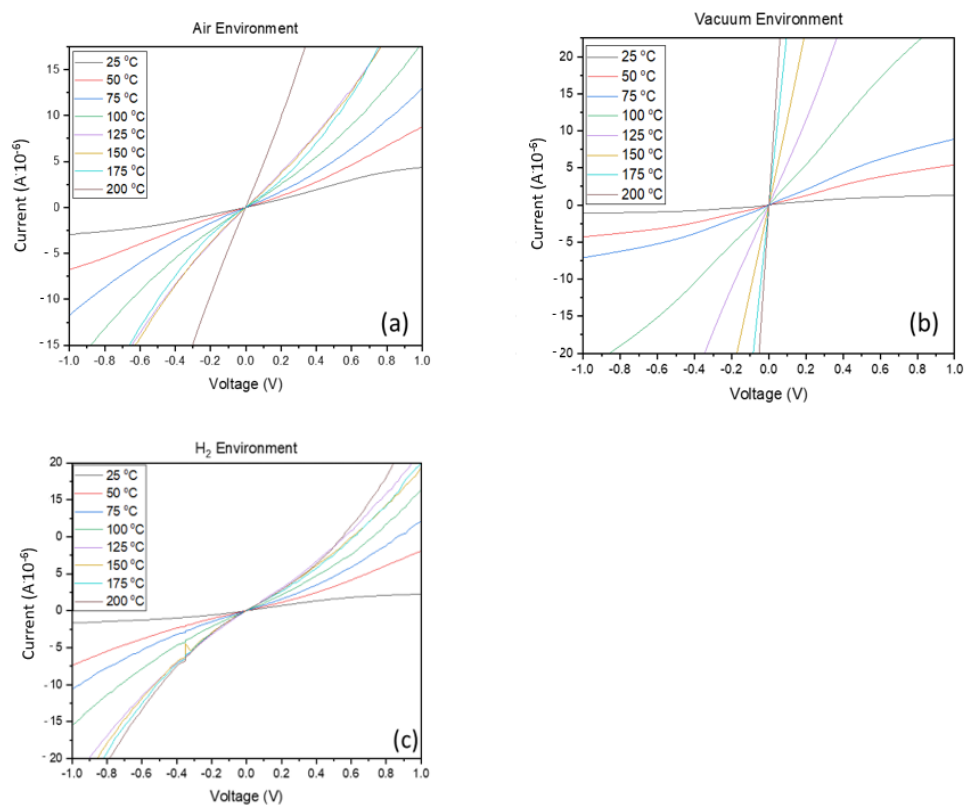


Figure 11. XPS spectra for (a) Sn-3d, (b) C-1s, (c) Cl-2p and (d) O-1s.

Table 1. Summary of the quantities in the undoped SnO₂.

	SnO ₂
Sn	1.0
O	1.94
Cl	0.02

**Figure 12.** The I–V characteristics of SnO₂ in (a) dry air, (b) a vacuum and (c) a hydrogen environment.

The activation energy E_a , defining the Fermi level E_F with respect to the conduction band bottom E_C , can be deduced from this plot:

$$\sigma = \sigma_0 \exp\left(\frac{-E_a}{k_B - T_h}\right), \quad E_a = E_C - E_F \quad (1)$$

where k_B is the Boltzmann constant and E_a is the overall activation energy of the conductance.

With this method, it is possible to obtain information about the activation energy, which is related to the conductance of semiconductor oxide sensors. To this end, the Arrhenius plot of the representative SnO₂ sample is given in Figure 13a in the three different chemical environments. The initial and final temperatures used in this study were 25 °C and 200 °C, respectively.

The value found for E_a here in dry air is around 0.37 eV (Figure 12). This value is nearer to the conduction band than to the mid-gap. The films here are therefore n-type semiconductors, which is in good agreement with the literature results [25,26] on such films. Much lower E_a values are obtained for films prepared at higher a T_S , which is somewhat independent of the molarity values. These large-grain crystallized films, as observed before from XRD and AFM, have better electrical conductivity due to enhanced carrier mobility. The hydrogen adsorption is seen to reduce the activation energy of SnO₂, reaching a value of 0.34 eV in the vacuum environment, which translates to the creation of more oxygen vacancies in the film and increases the activation energy to a value of 0.41 eV. Similar results

were also observed by Saukko and Lantto, where the exposure to hydrogen reduced the activation energy of the sample.

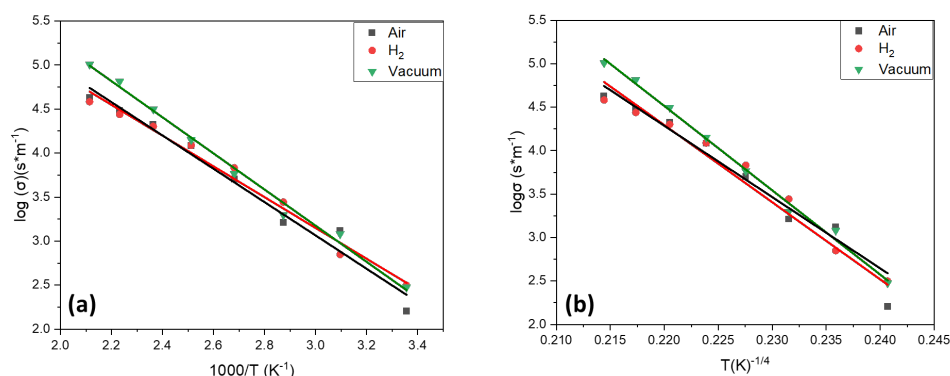


Figure 13. The Arrhenius plot of SnO₂ in dry air, a vacuum and a hydrogen environment as a function of (a) 1000/T and (b) 1/T^{1/4}.

To further analyze band structure changes in different chemical environments, we made an assessment of the low-temperature dc conductivity and its temperature dependence in the SnO₂ system using a variable range hopping (VRH) model [27,28]. According to this model, at low temperature the electrical transport consists of phonon-assisted hopping of charge carriers from occupied to unoccupied localized states. The theoretically predicted nearest-neighbor hopping conductivity, r , is given by the following formula:

$$\sigma = \sigma_0 \exp\left(-\frac{T_0}{T}\right)^{\frac{1}{4}} \quad (2)$$

After generating the Arrhenius plot (Figure 13b), we used the methodology described in similar works [29] to predict that the density of states at the Fermi level is increased upon hydrogen exposure and decreased in a vacuum environment. The results are presented in Table 2.

Table 2. The results from the VHR model.

Chemical Environment	Activation Energy (eV) ± 0.05 eV
Dry Air	0.37
Vacuum	0.40
H ₂	0.34

3. Materials and Methods

For all the computational simulations, the Cambridge Serial Total Energy Package (CASTEP) was used [30]. For the relaxation of the examined structures, we used the Perdew–Burke–Ernzerhof (PBE) functional [31], while for the electrical properties, we employed the hybrid PBE0 functional, with which we encountered the underestimation of the bandgap due to the effect of the localized electrons [32]. The sampling of the Brillouin zone was achieved with a k-point mesh of 2 × 2 × 3 k-points, while for the DOS calculations, we chose a set of 4 × 4 × 4 points.

The pristine SnO₂ sample was deposited by using the spin-coating method for the SnO₂ solutions. For the preparation of the undoped samples, we dissolved 0.045 g SnCl₂·2H₂O in 2 mL absolute ethanol. The solution was continuously stirred at 500 rpm for 24 h at room temperature. The sensor devices were deposited on the Si substrate as follows: The solution was coated on Si at an angular speed of 3000 rpm for 30 s, and then the substrate was dried at 110 °C for 10 min. This procedure was repeated 10 times. After the ten-layer deposition, the sample was left to crystallize at 500 °C for 2 h. Lastly, we used the e-beam

evaporation technique to deposit a thin layer of Pt on SnO₂ as a catalyst. The deposition lasted for 20 s and resulted in the creation of small Pt atoms on the material. With these Pt atoms the activation of the sensor occurs, which means that more adsorbed oxygen molecules are attracted, and the gas sensor thus reduces its response time when the gas is introduced. Practically, with Pt atoms on the surface, the band-structure of the surface changes with the creation of gap states, which attract more oxygen atoms from the dry air.

4. Conclusions

In this study, we extensively investigated the interaction of SnO₂ with dry air, a vacuum and hydrogen, both from a theoretical and an experimental point of view. In brief, we used DFT and studied the effect of intrinsic defects as well as of unintentional defects contained in the precursors. We found that unintentional dopants have a significant effect on the electronic properties of SnO₂; thus the gap states that are created can be of use in gas-sensing applications. Regarding the surface of SnO₂, we predicted that when hydrogen molecules are adsorbed onto the surface of SnO₂, gap states are created, which are responsible for the change in the resistance of the sample. To gain a better understanding of the effect of temperature on the sensing mechanism, as well as of the changes in some band-structure parameters, we applied the variable range hopping model in different environments and found that the response of the sensor also translates to a change in the activation energy and the density of states at the Fermi level. As predicted, the activation energy of resistance at different temperatures is increased when the material is placed in a vacuum environment, while it is decreased when the material is placed in a hydrogen environment. This work provides a better understanding of the sensing mechanism and connects it to the changes in the band structure.

Author Contributions: P.-P.F. and N.K. performed the DFT calculations; P.-P.F., A.S., C.D. and S.K. performed the experimental work; P.-P.F., N.K., M.V. and A.C. wrote the paper; M.V., A.S. and D.D. contributed to the analysis and discussion of the results. All authors have read and agreed to the published version of the manuscript.

Funding: This research received no external funding.

Institutional Review Board Statement: Not applicable.

Informed Consent Statement: Not applicable.

Data Availability Statement: Not applicable.

Acknowledgments: P.-P.F., A.C. and N.K. are grateful for funding from the Lloyd's Register Foundation, a charitable foundation helping to protect life and property by supporting engineering-related education, public engagement, and the application of research.

Conflicts of Interest: The authors declare no conflict of interest.

References

1. Heilig, A.; Bársan, N.; Weimar, U.; Schweizer-Berberich, M.; Gardner, J.; Göpel, W. Gas identification by modulating temperatures of SnO₂-based thick film sensors. *Sens. Actuators B Chem.* **1997**, *43*, 45–51. [[CrossRef](#)]
2. Lee, S.H.; Hoffman, D.M.; Jacobson, A.J.; Lee, T.R. Transparent, Homogeneous Tin Oxide (SnO₂) Thin Films Containing SnO₂-Coated Gold Nanoparticles. *Chem. Mater.* **2013**, *25*, 4697–4702. [[CrossRef](#)]
3. Dai, Z.R.; Pan, Z.W.; Wang, Z.L. Growth and Structure Evolution of Novel Tin Oxide Diskettes. *J. Am. Chem. Soc.* **2002**, *124*, 8673–8680. [[CrossRef](#)]
4. Batzill, M.; Diebold, U. The surface and materials science of tin oxide. *Prog. Surf. Sci.* **2005**, *79*, 47–154. [[CrossRef](#)]
5. Ghoshtagore, R.N. Mechanism of CVD Thin Film SnO₂ Formation. *J. Electrochem. Soc.* **1978**, *125*, 110–117. [[CrossRef](#)]
6. Wang, H.; Rogach, A.L. Hierarchical SnO₂ Nanostructures: Recent Advances in Design, Synthesis, and Applications. *Chem. Mater.* **2014**, *26*, 123–133. [[CrossRef](#)]
7. Takenaka, S.; Takahashi, R.; Sato, S.; Sodesawa, T.; Matsumoto, F.; Yoshida, S. Pore size control of mesoporous SnO₂ prepared by using stearic acid. *Microporous Mesoporous Mater.* **2003**, *59*, 123–131. [[CrossRef](#)]
8. Xu, C.; Tamaki, J.; Miura, N.; Yamazoe, N. Grain size effects on gas sensitivity of porous SnO₂-based elements. *Sens. Actuators B Chem.* **1991**, *3*, 147–155. [[CrossRef](#)]

9. Ponce, M.A.; Aldao, C.M.; Castro, M.S. Influence of particle size on the conductance of SnO₂ thick films. *J. Eur. Ceram. Soc.* **2003**, *23*, 2105–2111. [[CrossRef](#)]
10. Messad, A.; Bruneaux, J.; Cachet, H.; Froment, M. Analysis of the effects of substrate temperature, concentration of tin chloride and nature of dopants on the structural and electrical properties of sprayed SnO₂ films. *J. Mater. Sci.* **1994**, *29*, 5095–5103. [[CrossRef](#)]
11. Volintiru, I.; de Graaf, A.; van Deelen, J.; Poedt, P. The influence of methanol addition during the film growth of SnO₂ by atmospheric pressure chemical vapor deposition. *Thin Solid Films* **2011**, *519*, 6258–6263. [[CrossRef](#)]
12. Petaroudis, C.; Kostis, I.; Filippatos, P.-P.; Chroneos, A.; Soultati, A.; Vasilopoulou, M.; Davazoglou, D. Influence of thermal cycling on the optical and the electrical properties of atmospheric pressure chemical vapor deposited tin oxide films grown using water and methanol vapors as oxidizers. *Thin Solid Films* **2021**, *734*, 138841. [[CrossRef](#)]
13. Lu, P.-F.; Shen, Y.; Yu, Z.-Y.; Zhao, L.; Li, Q.-Y.; Ma, S.-J.; Han, L.-H.; Liu, Y.-M. Electronic Structure and Optical Properties of Antimony-Doped SnO₂ from First-Principle Study. *Commun. Theor. Phys.* **2012**, *57*, 145–150. [[CrossRef](#)]
14. Filippatos, P.-P.; Kelaidis, N.; Vasilopoulou, M.; Davazoglou, D.; Chroneos, A. Defect Processes in Halogen Doped SnO₂. *Appl. Sci.* **2021**, *11*, 551. [[CrossRef](#)]
15. Hoa Hong, N.; Song, J.-H.; Raghavender, A.T.; Asaeda, T.; Kurisu, M. Ferromagnetism in C-doped SnO₂ thin films. *Appl. Phys. Lett.* **2011**, *99*, 052505. [[CrossRef](#)]
16. Zervos, M.; Lathiotakis, N.; Kelaidis, N.; Othonos, A.; Tanasae, E.; Vasilee, E. Epitaxial highly ordered Sb:SnO₂ nanowires grown by the vapor liquid solid mechanism on m-, r- and a-Al₂O₃. *Nanoscale Adv.* **2019**, *1*, 1980–1990. [[CrossRef](#)]
17. Filippatos, P.-P.; Kelaidis, N.; Vasilopoulou, M.; Davazoglou, D.; Chroneos, A. Atomic structure and electronic properties of hydrogenated X (=C, Si, Ge, and Sn) doped TiO₂: A theoretical perspective. *AIP Adv.* **2020**, *10*, 115316. [[CrossRef](#)]
18. Brousse, T.; Schleich, D.M. Sprayed and thermally evaporated SnO₂ thin films for ethanol sensors. *Sens. Actuators B Chem.* **1996**, *31*, 77–79. [[CrossRef](#)]
19. Ren, X.; Liu, Y.; Lee, D.G.; Kim, W.B.; Han, G.S.; Jung, H.S.; Liu, S. Chlorine-modified SnO₂ electron transport layer for high-efficiency perovskite solar cells. *InfoMat* **2020**, *2*, 401–408. [[CrossRef](#)]
20. Vincent, C.A. The Nature of Semiconductivity in Polycrystalline Tin Oxide. *J. Electrochem. Soc.* **1972**, *119*, 515. [[CrossRef](#)]
21. Afify, H.H.; Momtaz, R.S.; Badawy, W.A.; Nasser, S.A. Some physical properties of fluorine-doped SnO₂ films prepared by spray pyrolysis. *J. Mater. Sci. Mater. Electron.* **1991**, *2*, 40–45. [[CrossRef](#)]
22. Yakuphanoglu, F. Electrical conductivity, Seebeck coefficient and optical properties of SnO₂ film deposited on ITO by dip coating. *J. Alloys Compd.* **2009**, *470*, 55–59. [[CrossRef](#)]
23. Filippatos, P.-P.; Kelaidis, N.; Vasilopoulou, M.; Davazoglou, D.; Lathiotakis, N.N.; Chroneos, A. Defect processes in F and Cl doped anatase TiO₂. *Sci. Rep.* **2019**, *9*, 19970. [[CrossRef](#)] [[PubMed](#)]
24. Rasheed, R.T.; Al-Algawi, S.D. Annealing Effect of SnO₂ Nanoparticles Prepared by the Sol–Gel Method. *J. Adv. Phys.* **2016**, *5*, 236–240. [[CrossRef](#)]
25. Lv, Y.; Han, C.; Zhu, Y.; Zhang, T.; Yao, S.; He, Z.; Dai, L.; Wang, L. Recent advances in metals and metal oxides as catalysts for vanadium redox flow battery: Properties, structures, and perspectives. *J. Mater. Sci. Technol.* **2021**, *75*, 96–109. [[CrossRef](#)]
26. Filippatos, P.-P.; Sharma, R.; Soultati, A.; Kelaidis, N.; Petaroudis, C.; Alivisatou, A.-A.; Drivas, C.; Kennou, S.; Christopoulos, S.-R.G.; Davazoglou, D.; et al. Optimization of the hydrogen response characteristics of halogen-doped SnO₂. *Sci. Rep.* **2023**, *13*, 2524. [[CrossRef](#)] [[PubMed](#)]
27. Myong, S.Y.; Lim, K.S. Universal single-phonon variable range hopping conduction for inorganic semiconducting polycrystalline films. *Appl. Phys. Lett.* **2006**, *88*, 222110. [[CrossRef](#)]
28. Mott, N.F. Conduction in glasses containing transition metal ions. *J. Non-Cryst. Solids* **1968**, *1*, 1–17. [[CrossRef](#)]
29. Plugaru, R.; Sandu, T.; Plugaru, N. First principles study and variable range hopping conductivity in disordered Al/Ti/Mn-doped ZnO. *Results Phys.* **2012**, *2*, 190–197. [[CrossRef](#)]
30. Segall, M.D.; Lindan, P.J.D.; Probert, M.J.; Pickard, C.J.; Hasnip, P.J.; Clark, S.J.; Payne, M.C. First-principles simulation: Ideas, illustrations and the CASTEP code. *J. Phys. Condens. Matter* **2002**, *14*, 2717–2744. [[CrossRef](#)]
31. Perdew, J.P.; Burke, K.; Ernzerhof, M. Generalized Gradient Approximation Made Simple. *Phys. Rev. Lett.* **1996**, *77*, 3865–3868. [[CrossRef](#)] [[PubMed](#)]
32. Paier, J.; Marsman, M.; Hummer, K.; Kresse, G.; Gerber, I.; Ángyán, J.G. Screened hybrid density functionals applied to solids. *J. Chem. Phys.* **2006**, *124*, 154709. [[CrossRef](#)] [[PubMed](#)]

Disclaimer/Publisher’s Note: The statements, opinions and data contained in all publications are solely those of the individual author(s) and contributor(s) and not of MDPI and/or the editor(s). MDPI and/or the editor(s) disclaim responsibility for any injury to people or property resulting from any ideas, methods, instructions or products referred to in the content.